Bulletin of Geophysics and Oceanography Vol. XX, n. X, pp. XXX-XXX; Xxxxx 20xx
DOI 10.4430/bgo00477

3D P-wave and S-wave velocity model for the characterisation of the subsurface beneath the village of Arquata del Tronto (central Italy)

G. Böhm, A. Affatato, G. Brancatelli, E. Forlin, F. Meneghini, L. Baradello and P. Corubolo

National Institute of Oceanography and Applied Geophysics - OGS, Trieste, Italy

(Received: 10 June 2024; accepted: 10 September 2024; published online: 18 October 2024)

ABSTRACT The geophysical characterisation of the subsurface in areas affected by strong earthquakes is a fundamental practice, which enables the correct assessment of seismic hazard and risk. In this study, we have considered the area of the historical centre of Arquata del Tronto (central Apennines, Italy), which was destroyed by a strong earthquake in 2016. A three dimensional (3D) P-wave and S-wave velocity model was defined and the model was obtained from first arrival tomography, computed on a seismic survey consisting of three lines hugging the hill where the old village was located. The velocity model and, especially, the V_P/V_S ratio show some interesting aspects, indicating in particular some anisotropic features present in the area due to the existence of flysch formations characterised by the alternation of sandstone, pelite, and marl in different proportions. In this analysis, the vertical seismic profile data acquired in a 100-metre deep borehole was also considered. The P-wave and S-wave vertical velocities were compared with the vertical velocities extracted from the 3D tomographic model at the same point of the well.

Key words: near surface, diving wave tomography, 3D velocity model, S wave.

1. Introduction

On 24 August 2016, the central region of Italy (central Apennines) was affected by an earthquake sequence with the mainshock being of magnitude M_W 6.0 (Pucci *et al.*, 2017) that caused heavy damage in this area. In particular, some villages such as Amatrice, Accumoli, and Arquata were almost completely destroyed (Vignola *et al.*, 2019; Brando *et al.*, 2020).

This work describes the results of a High Resolution Seismic (HRS) survey (P-wave and S-wave survey) carried out at the Arquata del Tronto (in the province of Ascoli Piceno) site, as part of the public intervention *"Progetto di suolo (terrazzamenti)"* [Soil project (terracing)] in the historical centre of Arquata del Tronto, funded by the Special Reconstruction Department of the Marche Region (USR), Italy. The aim of this work was the geophysical characterisation of the subsurface in order to define an accurate three-dimensional (3D) numerical velocity model for the modelling of the local seismic response through appropriate numerical simulations, in particular the identification of boundaries between lithostratigraphic units with different physical properties and their geometries, with the possible presence of faults. In this specific case, seismic investigations aimed to illuminate the shallowest part of the subsurface through the use of both compressional P waves and shear S waves. S waves have the great advantage of travelling at lower velocities compared to P waves and, at the same frequency, they have a

shorter wavelength and, thus, greater resolving power (Stümpel *et al*., 1984; Krawczyk *et al*., 2013; Pugin *et al*., 2013; Burschil *et al*., 2015; Chen *et al*., 2017). The final product of this study is a 3D velocity model obtained through traveltime tomography of the first arrivals picked from the acquired seismic data.

In Arquata, Pagliaroli *et al*. (2019b) obtained shear wave velocity ranging from 750 m/s to 1,000 m/s by integrating geological information with down-hole, Multichannel Analysis of Surface Waves (MASW), and Horizontal to Vertical Spectral Ratios (HVSR). Further geophysical investigations were carried out in the villages of Pretare and Piedilama using MASW and HVSR techniques (Imposa *et al*., 2017).

In the same area, Laurenzano *et al*. (2019), Giallini *et al*. (2020), and Primofiore *et al*. (2020) carried out analyses for the geophysical characterisation of the subsoil, which were based on the local seismic response on seismological data and used a numerical velocity model. On a local scale, they emphasised the different seismic behaviour of several sites around the Arquata del Tronto area. In particular, at the site of the Rocca di Arquata and the old village, they identified a probable topographic effect that led to a strong seismic amplification that caused the collapse of buildings. From a geological point of view, the Arquata del Tronto area is characterised by the Campotosto Member of the Laga Flysch Formation (Messinian), an arenaceous-pelitic sequence defined by three members with different sandstone prevailing lithofacies (Centamore *et al*., 1991; Artoni, 2003; Milli *et al*., 2007), with strikes of 5-10° and dips around 45° (Fig. 1). This formation is part of a WNW-ESE trending ridge in the central Apennine thrust-belt characterised by late Miocene lithofacies (Regione Marche, 2001). The village of Arquata is located on the elongated WNW–ESE trending ridge at 730 m a.s.l. (Fig. 2).

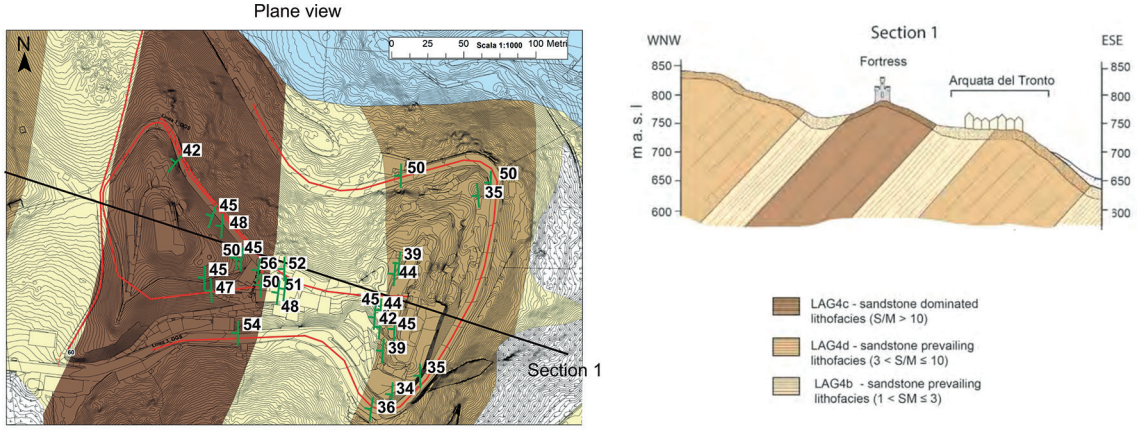

Fig. 1 - Geological map of the area (modified from Giallini *et al*., 2020). The red segments show the seismic survey used in this work. A vertical section, corresponding to the black line on the map, is shown on the right with the description of the geological formations in the area.

2. Seismic acquisition

The HRS survey in the municipality of Arquata consisted of three profiles (lines 1, 2, and 3) recorded in the second half of August 2023 (Fig. 2).

Lines 1 and 3 were surveyed with P and S waves using an electrodynamic vibrator (ELVIS VII) and a MiniVib IVI T-2500, while for line 2 only P waves were surveyed using a shotgun (ISOTTA)

with an 8-inch gauge. The choice of source type was based on the surface of the profiles: paved roadway (lines 1 and 3) and forest (line 2). The details of each profile surveyed are shown in Table 1.

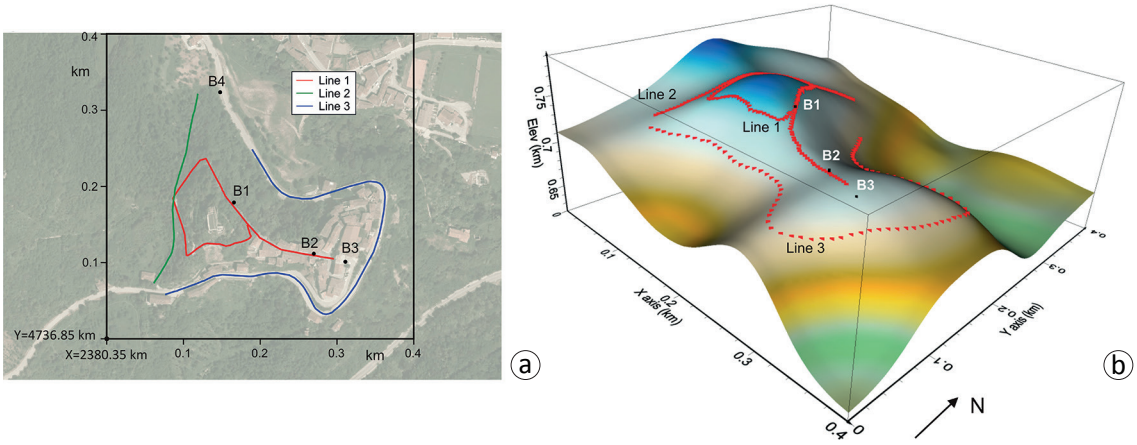

Fig. 2 - a) Location of the three seismic lines and the area used for the tomographic model (black rectangle) with the aerial image of the Arquata del Tronto area in transparency. The black dots represent the locations of the existing boreholes in this area (B1, B2, B3, and B4). The coordinates of the lower right vertex are given in the Monte Mario/ Italy Zone 2 reference system. b) 3D view of the line positions with respect to the topography of the area.

Table 1 - Details of the HRS acquisition.

Line	Source		Receiver	Spread
#1	ELVIS VII with sweep 20-220 Hz 10 s long (10% tapering). Two S-oriented energisations.	P mode	10 Hz vertical geophones	240 channels every 2 m and energisation every 4 m
		S mode	14 Hz horizontal geophones	
#2	Shotgun		10 Hz vertical geophones	134 channels every 2 m and energisation every 4 m
#3	ELVIS VII with sweep 20-220 Hz 10 s long and 10% tapering.	P mode	10 Hz vertical geophones	160 channels every 4 m and energisation every 8 m
	MiniVib IVI T-2500 with sweep 20-200 Hz 10 s long (10% tapering). One energisation.	S mode	14 Hz horizontal geophones	

The acquisition of the S waves of line 1 was divided into two parts (Fig. 3):

1) S1 mode, with the vibration source oriented at an angle of 5° N (corresponding to the average strike direction of the outcropped formations) and the geophones oriented at the same angle;
2) S2 mode, with the vibration source oriented at an angle of 95° N (perpendicular to the strike direction) and the geophones oriented at the same angle.

In these cases, the S1 or S2 acquisitions cannot be associated with SV- or SH-wave types. The arrival type of the S waves at the geophones depends on the position of the geophones with

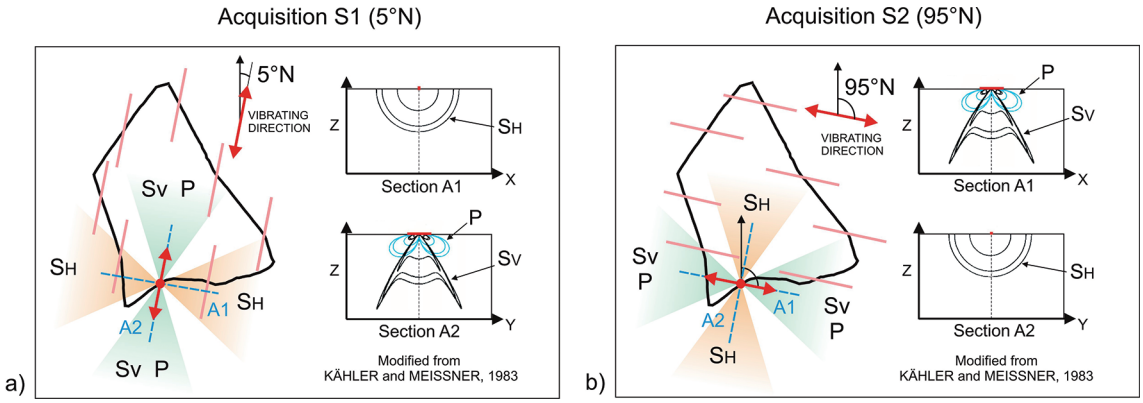

Fig. 3 - Two different S-wave acquisition schemes used for line 1: a) S1, S sources and S geophones oriented to 5° N; b) S2, S sources and S geophones oriented to 95° N. On the right side of each acquisition scheme, the two vertical sections, corresponding to the two directions of source vibration, show the different types of waves propagating in the two cases, S1 and S2. The SH waves propagate perpendicular to the direction of vibration (orange cones), while P and SV waves propagate in the same direction of the source vibration (green cones) with different angles from the surface (from Kähler and Meissner, 1983).

respect to the oscillation direction of the source. Fig. 3 shows that different types of waves are recorded at different receivers depending on the vibration direction of source S1 or S2. However, we can assume that the receivers of line 1, along the quasi-linear path (see the light blue line in Fig. 11), record pseudo SH arrivals for source S1, and pseudo SV arrivals for source S2.

For line 3, the S source was aligned perpendicularly to the local direction of the line and the geophones were all oriented at an angle of 5° N.

All seismic data were recorded using SUMMIT X one (DMT), a telemetric system specially developed for non-linear geometries.

In addition to the HRS campaign, a vertical seismic profile (VSP), with P and S waves, was recorded to calibrate the tomographic velocity model and compare the different velocities. The VSP study was carried out on existing borehole B2 (Fig. 2), which had the greatest depth (100 m) among the other existing boreholes in the area (30 m in B1, B3, and B4). ELVIS VII was used to generate both P and S waves recorded by the GSR-1 Slim geophone, which was internally equipped with an orthogonal triad of single OYO2400-15Hz geophones placed at 1-metre intervals in the borehole. Fig. 4 shows the vertical V_P and V_S values, obtained from the VSP analysis, and their ratio. The low value of the V_P/V_S ratio could be due to the combination of low effective pressure and small and irregular cracks, typical of the critical zone, which is characterised by low effective pressure and unconsolidated fracture media. In this case, the Poisson ratio could be negative ($V_P/V_S < 1.4$) (Flinchum *et al.*, 2024).

3. Seismic processing

This excerpt describes the challenges faced in seismic data processing due to low signal-to-noise (S/N) ratios caused by various sources of coherent noise. The data acquisition took place in an area characterised by a rough topography with lateral embankments, leading to lateral events that complicated signal interpretation. A specific processing sequence was employed to enhance signals in the data, with a focus on static corrections to address velocity variations in shallow subsurface layers and topographic elevation differences between sources and receivers.

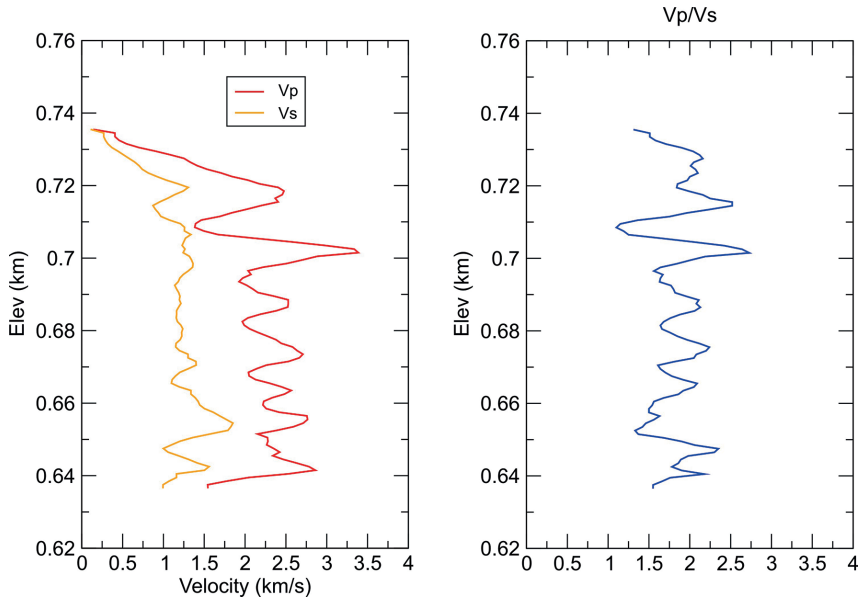

Fig. 4 - Instantaneous interval P-wave velocities (V_P = red line) and S-wave velocities (V_S = yellow line) computed from VSP data acquired in B2 (Fig. 2). The right panel shows the ratio between the V_P and V_S. Elevation is above sea level.

Two or four energisations at the same point were used to improve the S/N ratio through vertical stacking of recorded traces, with noisy traces removed beforehand (Duan *et al*., 2023). In geometry assignment, topographic coordinates and elevations obtained from field surveys were allocated to both receivers and sources across different lines of acquisition. By analysing the layout of active sources and receivers, the distribution of common depth points (CDPs) and their folds were determined. However, due to the non-linear course of line 1 and 2, the theoretical points, halfway between sources and receivers, sometimes deviated greatly from the course of the line. To mitigate the influence of these off-line reflections during stacking, the traces within CDPs were reorganised using a binning operation. Traces falling within a 5-metre radius from the bin centre were grouped together (Fig. 5). Therefore, in the central part of the line, the traces with relatively long offsets were rejected in order to preserve the hyperbolic move-out (Mazzotti *et al*., 2000). A 5-metre distance was selected as, at a velocity of 1.2 km/s and frequency of approximately 100 Hz, the lateral resolution, defined as the Fresnel zone (Sheriff, 1991), is greater.

First break picking was performed on all shot gathers to identify direct and refracted wave arrivals, which were used for both tomographic inversion and computing static corrections. These corrections are crucial in accurately positioning seismic events in chronological order, taking into account wave velocity elevation and variation caused by the geological properties of the subsurface.

In the P-wave survey, the static corrections were carried out in two steps. In the first, shots and receivers were moved on a floating datum, representing a smoothed approximation of the topographic surface. In this way, it was possible to preserve the hyperbolic characteristics of the reflections and, therefore, perform a correct velocity analysis. After the CDP stack, the data were moved to the final datum. Since near-surface S-wave velocities are more homogeneous than P-wave velocities (Pugin *et al*., 2013), only the elevation static correction was applied in order to move receivers and sources to the final datum.

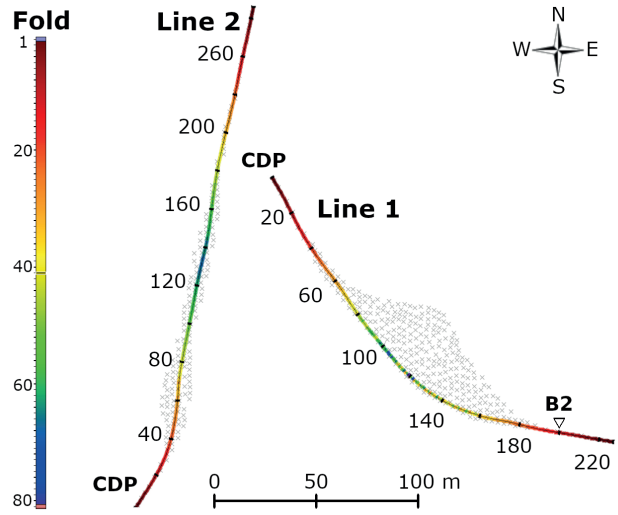

Fig. 5 - Calculation of CDPs and their coverage for lines 1 and 2, demonstrating that many points (grey dots) lie outside the line (especially for line 1). The maximum coverage in the central zone of the lines was approximately 80 traces per CDP.

To enhance the S/N ratio, a median filter was applied immediately after the first static correction step. Successively, a spherical divergence correction, using an average velocity function derived from a preliminary velocity analysis and a surface-consistent balancing, were performed to compensate for the amplitude decay and variations in receiver and source responses. Velocity analysis was performed every 20 CDPs. A specific mute function was defined to compensate for the stretching effects after the normal move-out correction.

Post-stack processing included FX deconvolution to attenuate incoherent noise and improve reflector continuity, time variant filtering, and final amplitude balancing. Ultimately, we applied a post-stack Kirchhoff time migration to line 1 P and line 1 S1, using the proper smoothed stacking velocity field scaled to 90 % to avoid artefacts. The final migrated images of line 1 S1 are compared with the time-converted P- and S-VSP functions (Figs. 6 and 7). Good agreement is observed with

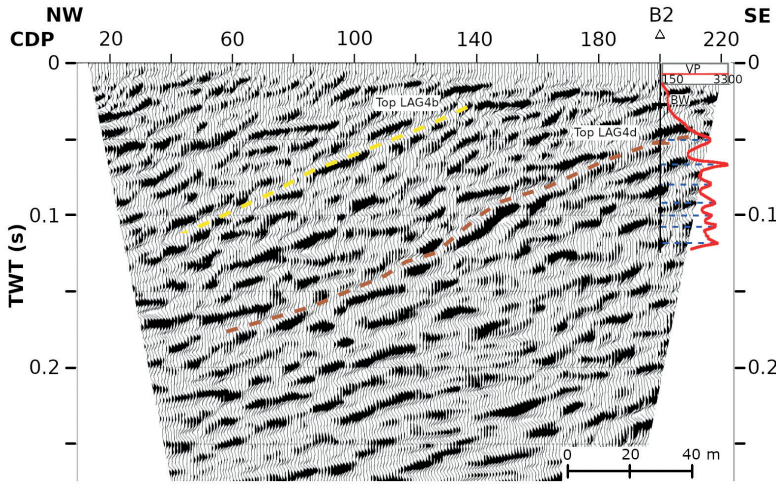

Fig. 6 - Post-stack migrated section of line 1 P with superimposed the P time-converted velocity from VSP data (red line). BW: base of weathering. The Top LAG 4d and Top LAG 4b horizons were interpreted as the tops of the respective lithofacies characterising the Campotosto Member of the Laga Flysch Formation.

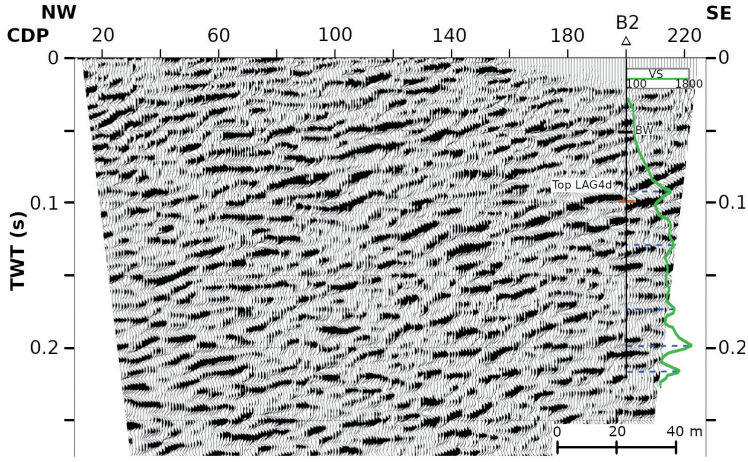

Fig. 7 - Post-stack migrated section of line 1 S1 with superimposed the S time-converted velocity from VSP data (green line). BW: base of weathering. Top LAG 4d: top of the respective lithofacies characterising the Campotosto Member of the Laga Flysch Formation.

the velocity picks and the principal seismic event interpreted as the top of the lithofacies LAG 4d (line 1P and line 1 S1 seismic sections) contrarily to the Top LAG 4b horizon interpreted on the basis of information reported in the literature [see Fig 1 modified from Giallini *et al*. (2020)]. The stacking image of line 2 shows sub-parallel partially continuous, high amplitude reflectors slightly down-dipping in the western part of the section (Fig. 8); the reflection pattern described above is consistent with the orientation of the line, which is almost parallel to the strike angle of the subsurface units (Fig. 1).

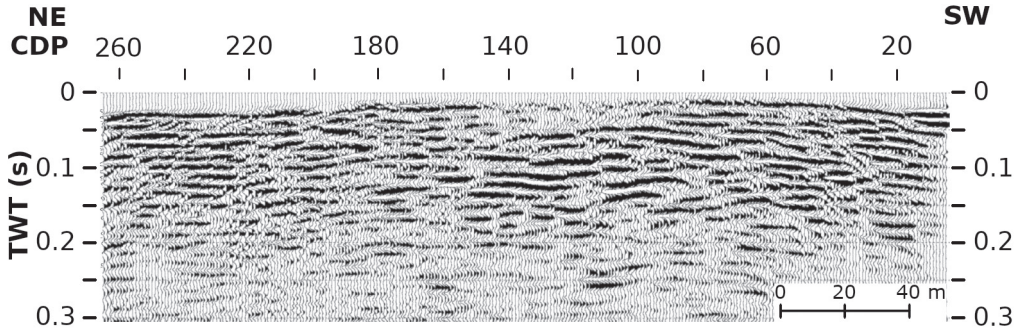

Fig. 8 - Stack section of line 2.

4. 3D velocity model

The 3D velocity model (Fig. 9) was obtained from the first arrival tomography, which was applied to all three seismic lines. All coordinates (related to Monte Mario - Italy zone 2, in the Gauss-Boaga projection) refer to a X = 0 Y = 0 origin, corresponding to point X = 2380.35 km and Y = 4736.85 km (Fig. 1). First arrival tomography was computed by means of the Cat3D software developed by OGS. The tomographic method used for these data is based on a ray tracing

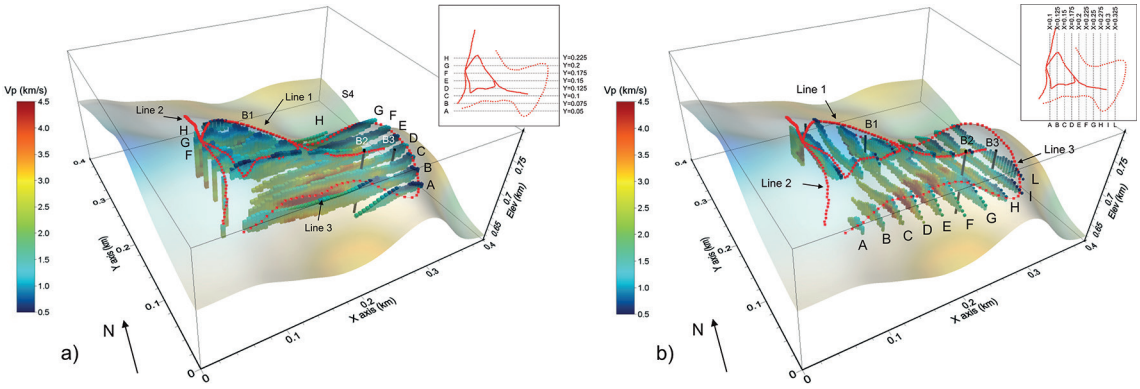

Fig. 9 - Two groups of vertical sections of the P-wave velocity volume shown in Fig. 7: a) sections along the E-W direction; b) sections along the N-S direction.

algorithm (Böhm *et al*., 1999) for the direct model and the iterative method SIRT (Simultaneous Iterative Reconstruction Technique) (Stewart, 1991) for the traveltime inversion. In addition, a model optimisation technique, based on the staggered grid method (Vesnaver and Böhm, 2000), was applied. This technique increases the resolution of the final inversion model by summing multiple tomographic solutions obtained from a starting grid shifted in the X and Y directions. The choice of the starting grid resolution must comply with a low null space condition, which is a measure of the high reliability of the tomographic solution and good conditioning of the tomographic system (resolution and ray coverage). Therefore, the final grid, obtained from the resampling and summation of each shifted output grid, has a higher resolution than the starting grid, while preserving the high reliability of the tomographic solution of the starting grid.

In general, seismic data acquired on land showed the presence of high level of coherent noise (mainly air waves and ground-roll) (Fig. 10). This is partly due to the presence of loose sediments or filling material below the surface (especially in the area of the old village) and the presence of walls, ditches, and trenches close to the survey lines, which, at times, led to interference in the data. For this reason, the interpretation and picking of the first arrivals used for the traveltime inversion was not easy, especially for the S-wave data. Nevertheless, a number of procedures were applied to improve the reliability of the picking, in particular the display of P-wave traveltime arrivals in the S-data records and their conversion to S-wave traveltime (using V_P/V_S = 1.73). Cross-checking of the picking in the common shot and common receiver domains, enabling a better control and management of the correct interpretation of the S arrivals, was also performed. The resolution of the final tomographic models for lines 1 and 2 is 2.5 m, in both the horizontal (X, Y) and vertical (Z) directions, after applying the staggered grid technique and starting from a base grid of 10x10 m (in X, Y). For line 3, the resolution of the final velocity model is 5 m (X, Y) per 2.5 m (Z), starting from an initial grid of 15x15 m (X, Y).

For each inversion, the reliability of the tomographic solution was checked by analysing the time residuals (difference between the observed traveltimes and the traveltimes calculated on the final model). In the inversions of the P traveltimes, the root mean square (RMS) for the time residuals was approximately 3.5% in relation to the observed times, corresponding approximately to 2.3 m/s for line 1, 3.1% corresponding to 1.5 m/s for line 2, and 1.6% corresponding to 1.3 m/s for line 3. The survey of line 1 includes a circular ring around the castle hill and a geophone line that follows the path leading to the centre of the old village. Fig. 11 shows an example of picking of the first P arrivals interpreted in a common shot section of the circular path (see the

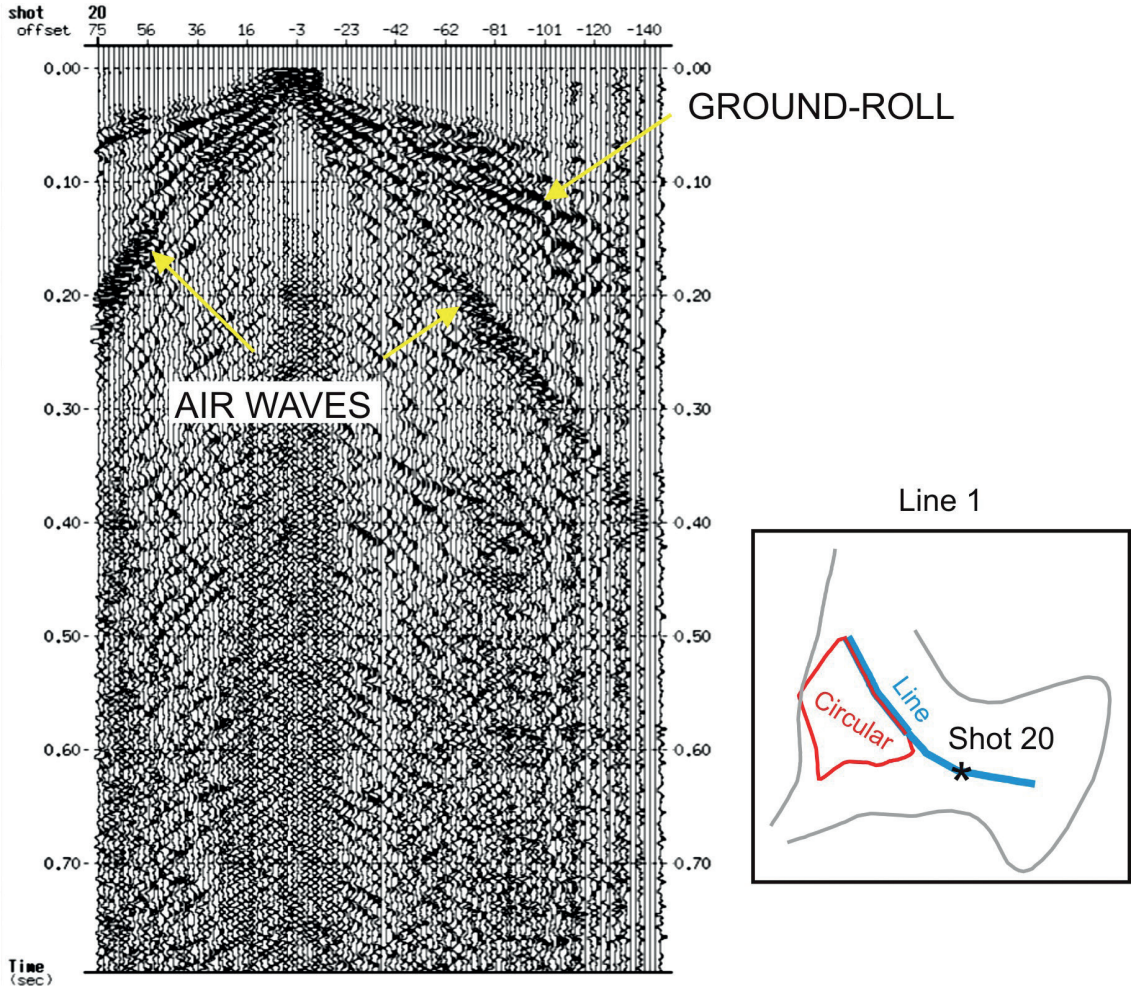

Fig. 10 - Common shot gather of line 1 P.

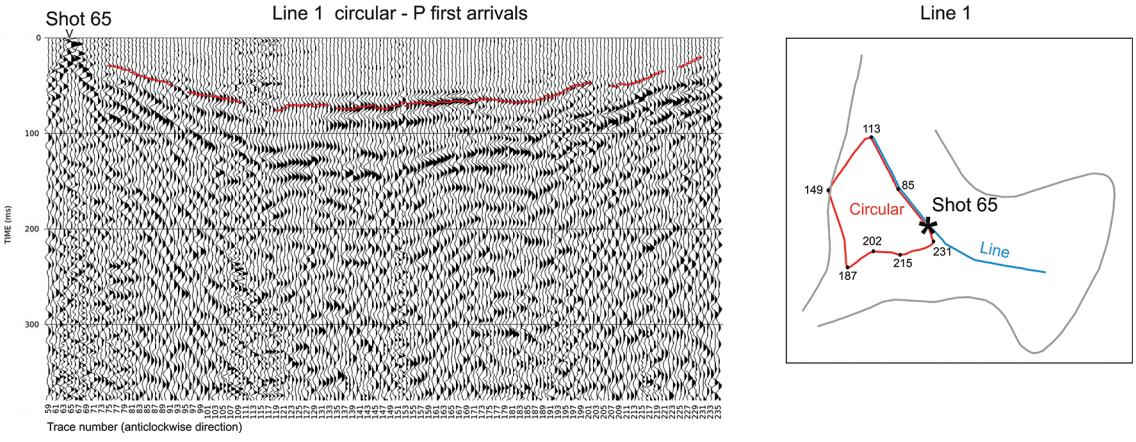

Fig. 11 - Picking of the first P arrivals (red dots) in a common shot section of the circular part of line 1. The star symbol indicates the position of the displayed shot. The trace numbers increase in a counterclockwise direction with respect to the circular geometry of acquisition.

star symbol on the right). In addition to the P arrivals, two S arrivals were recorded from two separate acquisitions (Fig. 12): the first (S1 in Fig. 12a) with both the sources and geophones oriented 5° N (Fig. 3a); the second (S2 in Fig. 12b) with both the sources and geophones oriented in a perpendicular direction 95° N (Fig. 3b).

The results of the first arrival tomography for line 1 are shown in Fig. 13 as horizontal sections of the P-wave and S-wave velocity fields at Z = 739 m, corresponding to a depth of 10 - 20 m from

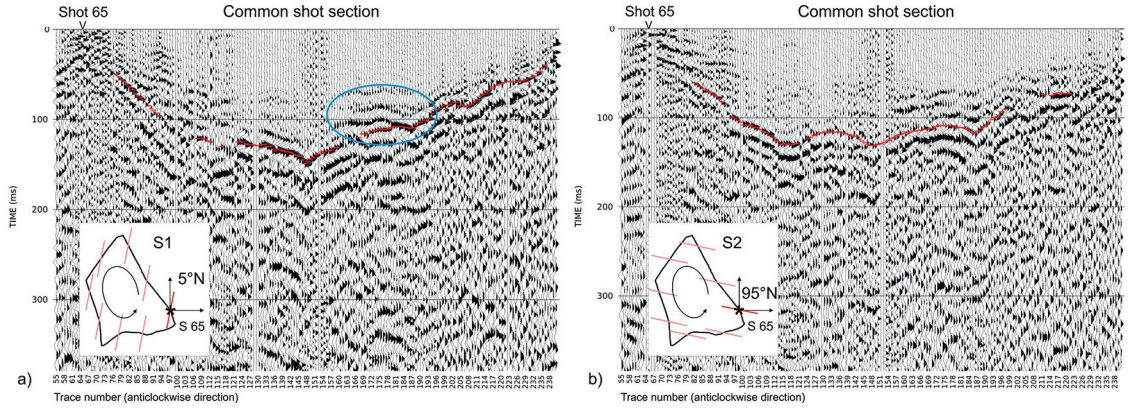

Fig. 12 - Picking of the first arrivals (red dots) for S1 (a) and S2 (b) on the same common shot section of the circular part of line 1. The trace numbers increase in a counterclockwise direction with respect to the circular geometry of acquisition. The blue circle indicates the presence of P-wave trains.

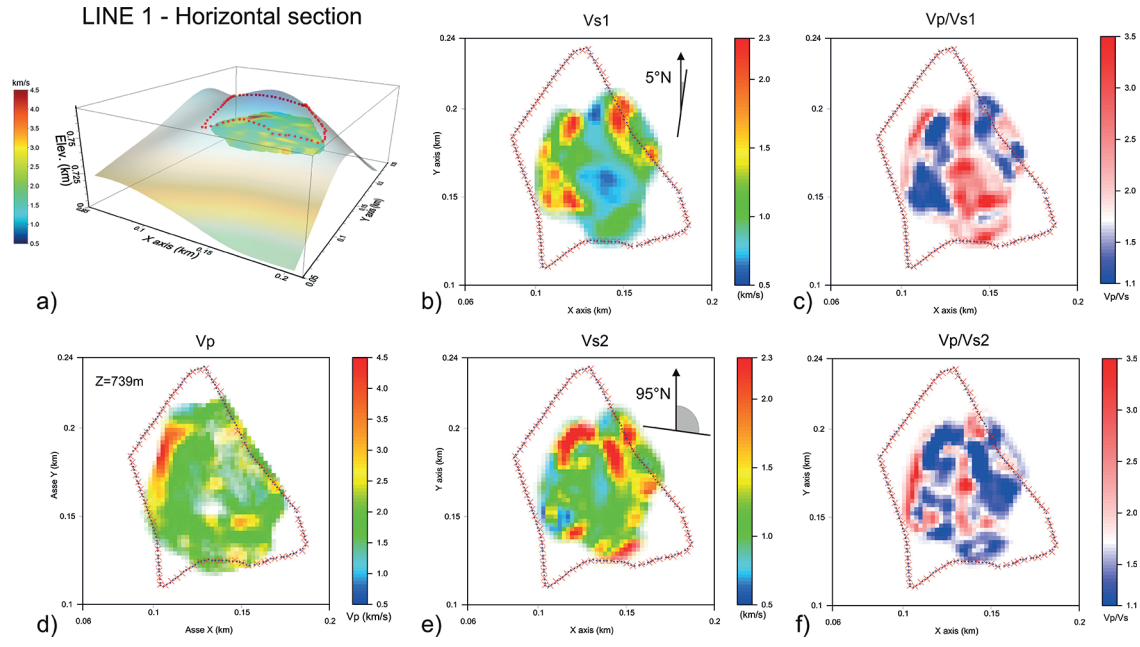

Fig. 13 - Velocity fields from the first arrival tomography of the circular part of line 1: a) 3D view of a horizontal section at Z = 739 m, which corresponds to a depth of approximately 10-20 m from the topography of the geophone line; b) S-wave velocity refers to acquisition S1; c) the corresponding V_P/V_S ratio on the same section in panel b; d) P-wave velocity; e) S-wave velocity refers to acquisition S2; f) the corresponding V_P/V_S ratio on the same section in panel e.

the topography on the geophone line. The P image (Fig. 13d) shows moderate heterogeneity, except for a zone of higher velocities on the left side. Both S velocities (Figs. 13b and 13e) show greater heterogeneity than the P velocities. In particular, the values at the border of the investigated area are higher than in the central part.

Line 2 was located on the left side of the survey area, next to the fortress hill. This line was acquired by using a shotgun as a source, with only P arrivals recorded (see Table 1 for details). Fig. 14a shows an example of first break picking in a common shot gather. The result of the first break tomography shows high velocities in almost the entire area investigated, even close to the surface (Fig. 14b).

Line 3 was acquired in the narrow road around the hill of the old village (Fig. 2). Here the source was the MiniVib for the P waves and the electrodynamic vibrator for the S waves (see Table 1 for details). Fig. 15 shows an example of first arrival picking in a common shot gather (Fig. 15a) and the 3D P-wave velocity volume from the diving wave tomography (Fig. 15b).

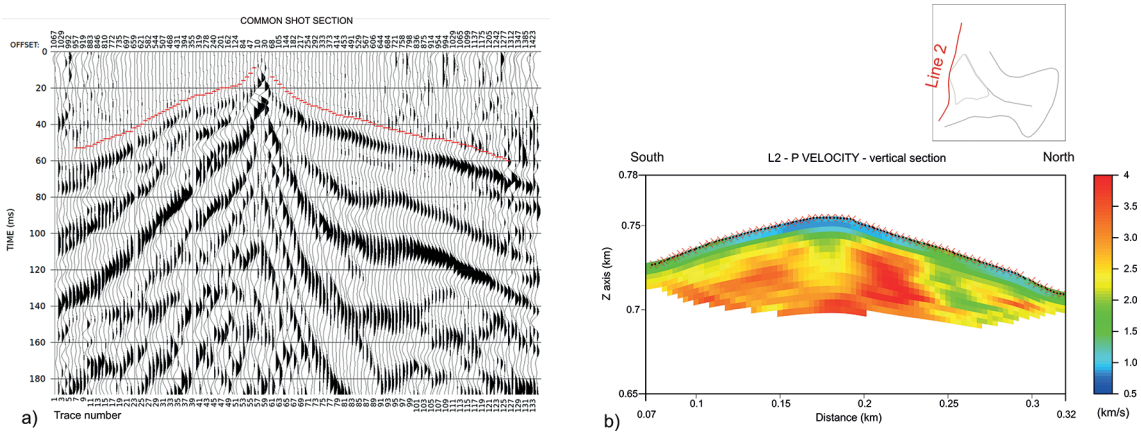

Fig. 14 - First arrival tomography of line 2: a) picking of P-wave first arrivals (first break) in a common shot section; b) vertical section of the P-wave velocity from tomography.

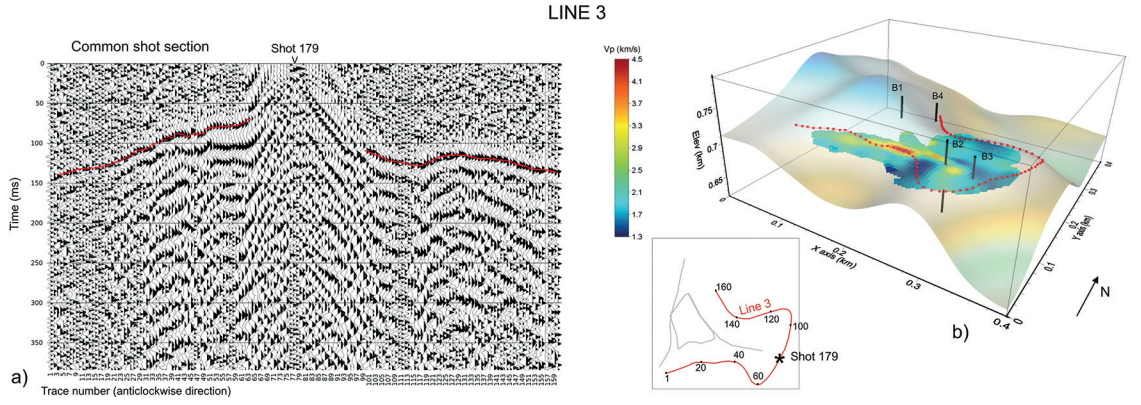

Fig. 15 - First arrival tomography of line 3: a) picking of P-wave first arrivals in a common shot section; b) 3D view of the P-wave velocity from tomography. The black bars are the positions of the boreholes performed in the area.

5. Results and conclusions

The velocity pattern obtained from the tomography of the first arrivals shows some interesting aspects. In the western part of the studied area, at line 2, the parts characterised by high P-wave velocities (3.5 - 4.0 km/s) almost reach the surface and have a thin overburden, confirming, in this part, the presence of lithofacies with a high proportion of sandstone (LAG 4c in Fig. 1). In the central part, the high-velocity zones are deeper and mainly present towards the west (Figs. 9 and 10), while in the area below the old village, in the eastern part of the study area, the P-wave velocities are lower even at depths of several tens of metres. As for the hill with ruins of the fortress (circular line 1), the velocities of both P and the two types of S (S1 and S2) show quite heterogeneous values, indicating a greater structural complexity of the rock in this part. The V_P/V_S ratio, especially the V_P/V_{S1} values (Fig. 13c), shows a pattern of alternating positive and negative values with respect to the reference value of 1.73 in the N-S direction, which is more clearly visible in line 3 (Fig. 16c), and also consistent with the orientation of the black planes in Fig. 17. This pattern can be associated with the presence of alternating more compact flysch beds (low V_P/V_S) and adjacent less compact and more fractured beds (high V_P/V_S), since V_P is more sensitive to the fracture density and fluid saturation than V_S (Ding *et al.*, 2018; Flinchum *et al.*, 2024).

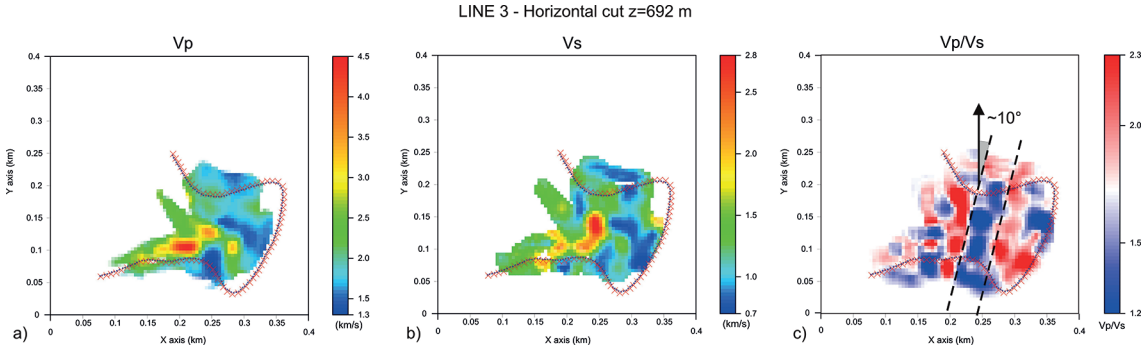

Fig. 16 - Horizontal section of the first arrival tomography of line 3: P-wave velocity (a), S-wave velocity (b), V_P/V_S ratio (c).

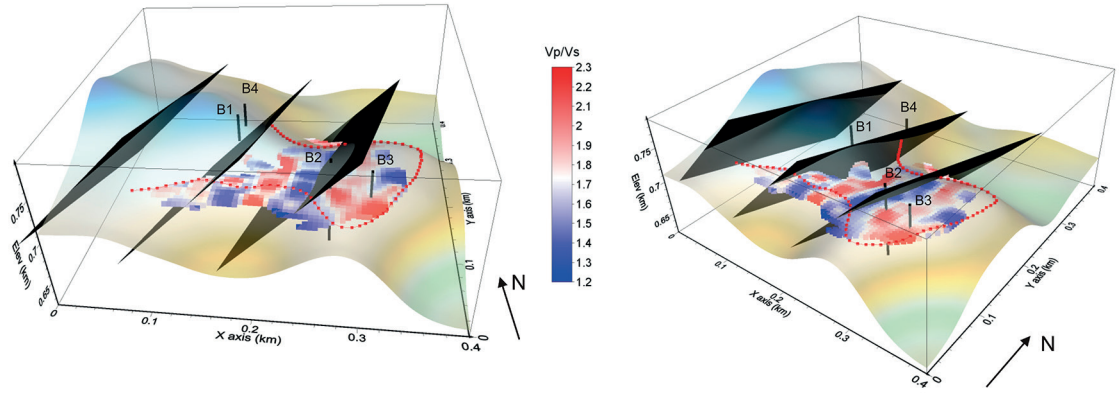

Fig. 17 - Horizontal section of the V_P/V_S ratio of line 3 (Fig. 16 c), displayed in a 3D view related with the orientation of the hypothetical planes of the buried formations in this area (black planes).

In Fig. 18, we can observe the vertical variation of the P-wave velocity at different depths from the topography extracted from the total 3D model. These images confirm the presence of a higher P-wave velocity at a depth of 20-30 m below the topography, in the southern part of the area and in correspondence of line 2. Whereas in the eastern part, below the old village, the P-wave velocity remains lower even at a depth of 40 m below the surface.

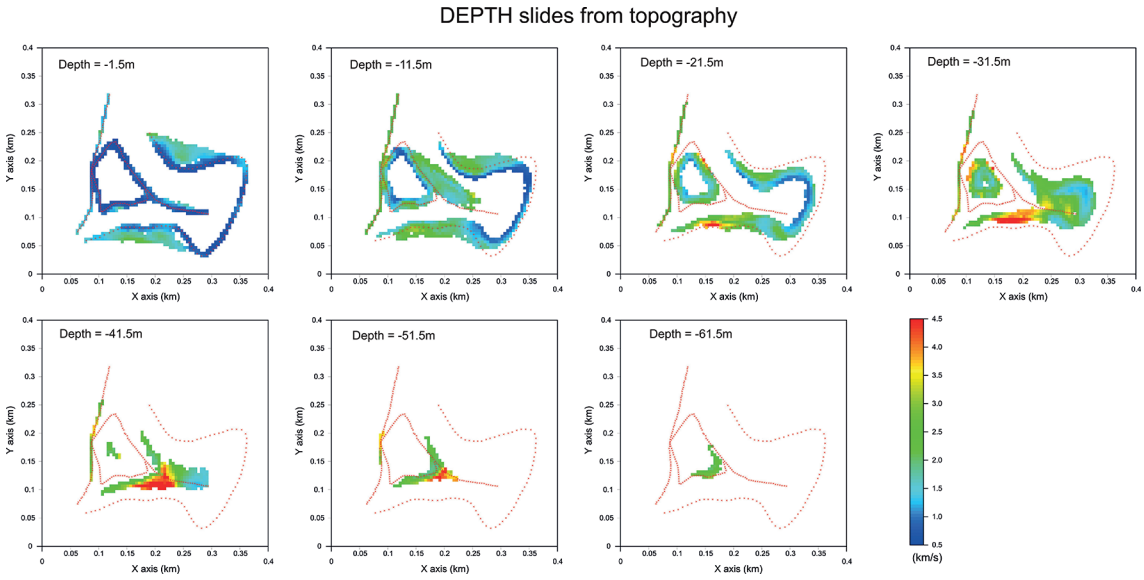

Fig. 18 - Horizontal slices corresponding to the different depths of the final 3D tomographic P-wave velocity model with respect to the topographic quota of the corresponding geophones.

The vertical P-wave velocities from the B2 VSP data were also compared with the P-wave velocities extracted from the 3D model obtained from the diving tomography of line 3 and the P-wave velocities from the direct tomography of the VSP data (Fig. 19). The tomography from the VSP data (red curve) was obtained by means of the traveltime inversion of the first arrival picked on the VSP data using a model with horizontal layers with a 5-metre thickness. The vacancy in the velocity of this curve is due to the lack of picking times as a result of the low reliability of the data at the corresponding depth. The general trend of the diving tomographic results (green line) is consistent with the VSP curve (yellow line), except for a difference in the velocity values, which could be due to the different directions of investigation for the two results. First arrival tomography uses the diving ray paths that mainly correspond to the sub-horizontal rays in the area below the well, where the diving ray paths reach their maximum depth relative to the source and receiver position, and the ray angles are inclined by less than 15° to the XY plane due to the characteristic geometry of the diving wave ray path. Conversely, the direction of investigation is vertical in the VSP analysis. Thus, we can assume that the difference in velocity between tomography and VSP is due to the presence of anisotropy in the flysch formation. Indeed, in an anisotropic layer, the velocity of a wave propagating parallel to the sedimentation planes is higher than the velocity of a wave propagating in a perpendicular direction. Since the velocities associated with VSP are greater than the velocities of sub-horizontal rays (diving tomography), the dip angle of the layers can be assumed to be greater than 45°, as, in this case, the vertical direction is closer to the plane orientation of the layers (higher velocity) and the horizontal

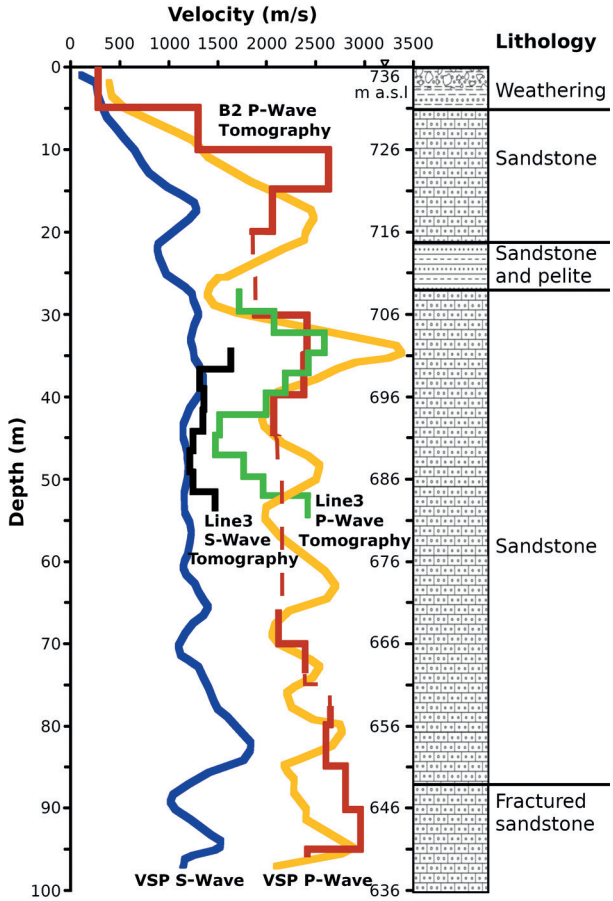

Fig. 19 - Comparison between the P and S velocities from VSP data (yellow and blue line), vertical functions V_P and V_S (green and black line) extracted from the tomographic model of line 3 at the position of B2, and the P-wave velocity computed by tomography of the VSP data (red line). The dashed red segments indicate the not picked part in the VSP section.

direction is closer to the perpendicular direction (lower velocity). This is the condition that could justify the higher velocity of the VSP compared to the velocity obtained from tomography. The V_S values calculated from the VSP data show weak fluctuations and well agree with the values reported by Pagliaroli *et al*. (2019a), i.e. V_S 1000 m/s for LAG 4c-d and 900 m/s for LAG 4b.

In conclusion, in this paper we have presented the results of the tomographic inversion of the first arrivals related to three surface seismic lines, with which we have obtained a volume of P- and S-wave velocities that highlights some interesting aspects of the subsurface in the area of the old village of Arquata del Tronto, hit in 2016 by a strong earthquake that practically destroyed the entire village. Despite great difficulties in the interpretation and picking of the first arrivals used for the inversion, especially for the S data, we have characterised part of the subsurface through variations of V_P, V_S, and their V_P/V_S ratio within the study area and compared it with the known geology of the area.

Acknowledgments. The authors express their gratitude to the entire OGS acquisition group for the professional level demonstrated in the tough acquisition task, the Special Reconstruction Department of the Marche Region (USR) for the permission to publish these data and results. A special thank you to Carlo G. Lai (Eucentre Foundation, Pavia), Alessandro Pagliaroli, and Alberto Pizzi of the University of Chieti, and to the IHS Markit® of S&P Global for the use of Kingdom™ and Echos™ software for seismic and VSP data interpretation and seismic processing. This work was presented at the 42nd National Conference of the GNGTS (Gruppo Nazionale di Geofisica della Terra Solida), 2024.

REFERENCES

Artoni A.; 2003: *Messinian events within the tectono-stratigraphixc evolution of the southern Laga basin (central Apennines, Italy).* Boll. Soc. Geol. It., 122, 447-465.

Böhm G., Rossi G. and Vesnaver A.; 1999: *Minimum-time ray tracing for 3-D irregular grids*. J. Seismic Explor., 8, 117-131.

Brando G., Pagliaroli A., Cocco G. and Di Buccio F.; 2020: *Site effects and damage scenarios: the case study of two historic centers following the 2016 central Italy earthquake.* Eng. Geol., 272, doi: 10.1016/j.enggeo.2020.105647.

Burschil T., Beilecke T. and Krawczyk C.M.; 2015: *Finite-difference modelling to evaluate seismic P-wave and shear-wave field data.* Solid Earth, 6, 33-47.

Centamore E., Cantalamessa G., Micarelli A., Potetti M., Berti D., Bigi S., Morelli C. and Ridolfi M.; 1991: *Stratigrafia e analisi di facies dei depositi del Miocene e del Pliocene Inferiore dell'avanfossa marchigiano-abruzzese e delle zone limitrofe. Studi Geologici Camerti,* CROP 11, pp. 125-131.

Chen J., Zelt C.A. and Jaiswal P.; 2017: *Detecting a known near-surface target through application of frequency-dependent traveltime tomography and full-waveform inversion to P- and SH-wave seismic refraction data*. Geophys., 82, R1-R17, doi: 10.1190/geo2016-0085.1.GPYSA70016-8033.

Ding P., Wang D., Di G. and Li X.; 2018: *Investigation of the effects of fracture orientation and saturation on the Vp/Vs ratio and their implications.* Rock Mech. Rock Eng., 52, 3293-3304, doi: 10.1007/s00603-019-01770-3.

Duan H., Zhu P. and Peng S.; 2023: *Characteristic and processing method of SH-wave data generated by vibroseis source.* J. Appl. Geophys., 214, doi: 10.1016/j.jappgeo.2023.105052.

Flinchum B.A., Grana D., Carr B.J., Ravichandran N., Eppinger B. and Holbroo W.S.; 2024: *Low Vp/Vs values as an indicator for fractures in the critical zone.* Geophys. Res. Lett., 51, doi: 10.1029/2023GL105946.

Giallini S., Pizzi A., Pagliaroli A., Moscatelli M., Vignaroli G., Sirianni P., Mancini M. and Laurenzano G.; 2020: *Evaluation of complex site effects through experimental methods and numerical modelling: the case history of Arquata del Tronto, central Italy.* Eng. Geol., 272, doi: 10.1016/j.enggeo.2020.105646.

Imposa S., Panzera F., Grassi S., Lombardo G., Catalano S., Romagnoli G. and Tortorici G.; 2017: *Geophysical and geologic surveys of the areas struck by the August 26th 2016 central Italy earthquake: the study case of Pretare and Piedilama.* J. Appl. Geophys., 145, 17-27.

Kähler S. and Meissner R.; 1983: *Radiation and receiver pattern of shear and compressional waves as a function of Poisson's ratio*. Geophys. Prospect., 31, 421-435, doi: 10.1111/j.1365-2478.1983.tb01061.x.

Krawczyk C.M., Polom U. and Beilecke T.; 2013: *Shear-wave reflection seismics as a valuable tool for near-surface urban applications.* The Leading Edge, 32, 256-263, doi: 10.1190/tle32030256.1.

Laurenzano G., Barnaba C., Romano M.A., Priolo E., Bertoni M., Bragato P.L., Comelli P., Dreossi I. and Garbin M.; 2019: *The central Italy 2016-2017 seismic sequence: site response analysis based on seismological data in the Arquata del Tronto-Montegallo municipalities.* Bull. Earthquake Eng., 17, 5449-5469, doi: 10.1007/s10518-018-0355-3.

Mazzotti A., Stucchi E., Fradelizio G. L., Zanzi L. and Scandone P.; 2000: *Seismic exploration in complex terrains: a processing experience in the southern Apennines.* Geophysics, 65, 1402-1417, doi: 10.1190/1.1444830.

Milli S., Moscatelli M., Stanzione O. and Falcini F.; 2007: *Sedimentology and physical stratigraphy of the Messinian turbidite deposits of the Laga basin (central Apennines, Italy).* Boll. Soc. Geol. Ital., 126, 255-281.

Pagliaroli A., Gaudiosi I.; Razzano R., Giallini S., De Siva F., Chiaradonna A., Ciancimino A. and Foti S.; 2019a: *Site response analyses for seismic microzonation: case-histories, results and applications in central Italy.* In: Proc. 7th lnternational Conference on Earthquake Geotechnical Engineering (VII ICEGE), Roma, Italy, pp. 960-974.

Pagliaroli A., Pergalani F., Ciancimino A., Chiaradonna A., Compagnoni M., De Silva F., Foti S., Giallini S., Lanzo G., Lombardi F., Luzi L., Macerola L., Nocentini M., Pizzi A., Tallini M. and Teramo C.; 2019b: *Site response analyses for complex geological and morphological conditions: relevant case-histories from 3rd level seismic microzonation in central Italy*. Bull. Earthquake Eng., 18, 5741-5777, doi: 10.1007/s10518-019-00610-7.

Primofiore I., Baron J., Klin P., Laurenzano G., Muraro C., Capotorti F., Amanti M. and Vessia G.; 2020: *3D numerical modelling for interpreting topographic effects in rocky hills for Seismic Microzonation: the case study of Arquata del Tronto hamlet.* Eng. Geol., 279, doi: 10.1016/j.enggeo.2020.105868.

Pucci S., De Martini P.M., Civico R., Villani F., Nappi R., Ricci T., Azzaro R., Brunori C.A., Caciagli M., Cinti F.R., Sapia V., De Ritis R., Mazzarini F., Tarquini S., Gaudiosi G., Nave R., Alessio G., Smedile A., Alfonsi L., Cucci L. and Pantosti D.; 2017: *Coseismic ruptures of the 24 August 2016, Mw6.0 Amatrice earthquake (central Italy).* Geophys. Res. Lett., 44, 2138-2147, doi: 10.1002/2016GL071859.

Pugin A.J.M., Pullan S.E. and Hunter J.A.; 2013: *Shear-wave high-resolution seismic reflection in Ottawa and Quebec City, Canada.* The Leading Edge, 32, 250-255, doi: 10.1190/tle32030250.1.

Regione Marche; 2001: *Progetti CARG e Obiettivo 5B. P.F. Informazioni Territoriali.* <http://www.regione.marche.it/Regione-Utile/Paesaggio-Territorio-Urbanistica/Cartografia/Repertorio/Cartageologicaregionale10000>

Sheriff R.E.; 1991: *Encyclopedic dictionary of exploration geophysics (3rd ed.*). Soc. Explor. Geophys. (SEG), Houston, TX, USA, 384 pp.

Stewart R.; 1991: *Exploration seismic tomography: fundamental.* Soc. Explor. Geophys. (SEG), Houston, TX, USA, Course note series, vol. 3, 201 pp., doi: 10.1190/1.9781560802372.

Stümpel H., Kähler S., Meissner R. and Milkereit B.; 1984: *The use of seismic shear waves and compressional waves for lithological problems of shallow sediments*. Geophys. Prospect., 32, 662-675, doi: 10.1111/j.1365-2478.1984.tb01712.x.GPPRAR0016-8025.

Vesnaver A. and Böhm G.; 2000: *Staggered or adapted grids for seismic tomography?* The Leading Edge, 19, 944-950, doi: 10.1190/1.1438762.

Vignola L., Gallipoli M.R., Chiauzzi L., Stabile T.A., Piscitelli S., Santarsiero G., Bellanova J., Calamita G. and Perrone A.; 2019: *Geophysical and engineering analysis of different earthquake damage in Pescara del Tronto and Vezzano (Arquata del Tronto Municipality) following the 24th August 2016 central Italy earthquake.* Bull. Earthquake Eng., 17, 5471-5493, doi: 10.1007/s10518-018-0450-5.

Corresponding author: Gualtiero Böhm
National Institute of Oceanography and Applied Geophysics – OGS
Borgo Grotta Gigante 42c, 34010 Sgonico (TS), Italy
Phone: +39 040 2140295; email: gbohm@ogs.it